iScience

CellPress
OPEN ACCESS

Article

Use of dual-electron probes reveals the role of ferritin as an iron depot in *ex vivo* erythropoiesis

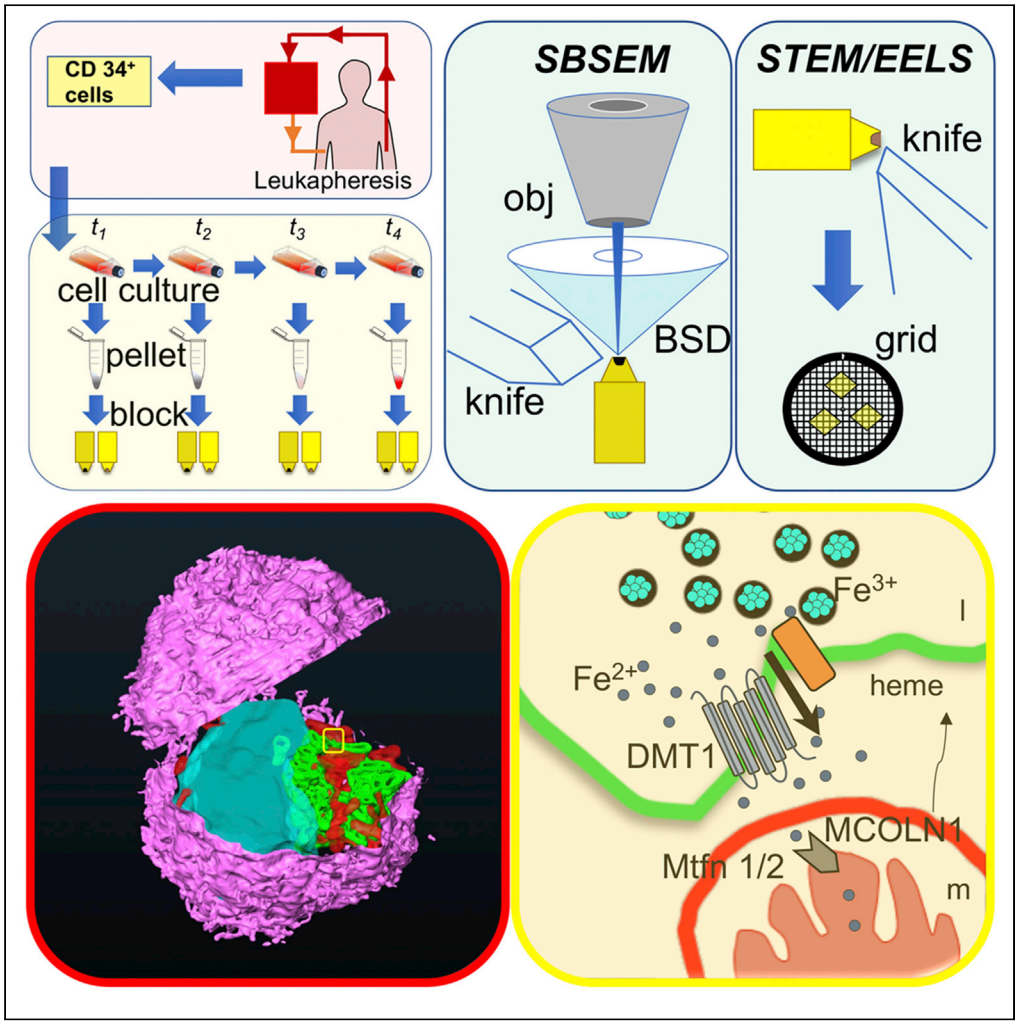

Maria A. Aronova, Seung-Jae Noh, Guofeng Zhang, Colleen Byrnes, Emily Riehm Meier, Young C. Kim, Richard D. Leapman

aronovaa@mail.nih.gov

Highlights

Erythroblasts maintain highly organized architecture as revealed by SB-SEM

STEM/EELS reveal ferritin-containing lysosomal vesicles surrounded by mitochondria

In erythropoiesis, ferritin is attributed to be an iron depot used in heme synthesis

Aronova et al., iScience *24*, 102901
August 20, 2021
https://doi.org/10.1016/j.isci.2021.102901

iScience

CellPress
OPEN ACCESS

Article

Use of dual-electron probes reveals the role of ferritin as an iron depot in *ex vivo* erythropoiesis

Maria A. Aronova,[1,6,*] Seung-Jae Noh,[2] Guofeng Zhang,[1] Colleen Byrnes,[3] Emily Riehm Meier,[4] Young C. Kim,[5] and Richard D. Leapman[1]

SUMMARY

In the finely regulated process of mammalian erythropoiesis, the path of the labile iron pool into mitochondria for heme production is not well understood. Existing models for erythropoiesis do not include a central role for the ubiquitous iron storage protein ferritin; one model proposes that incoming endosomal Fe^{3+} bound to transferrin enters the cytoplasm through an ion transporter after reduction to Fe^{2+} and is taken up into mitochondria through mitoferrin-1 transporter. Here, we apply a dual three-dimensional imaging and spectroscopic technique, based on scanned electron probes, to measure Fe^{3+} in *ex vivo* human hematopoietic stem cells. After seven days in culture, we observe cells displaying a highly specialized architecture with anchored clustering of mitochondria and massive accumulation of nanoparticles containing high iron concentrations localized to lysosomal storage depots, identified as ferritin. We hypothesize that lysosomal ferritin iron depots enable continued heme production after expulsion of most of the cellular machinery.

INTRODUCTION

Although light microscopy (LM) and immuno-electron microscopy (EM) offer powerful approaches to improve our understanding of cellular pathways through the identification of specific fluorescently tagged proteins, or Au-antibody-labeled proteins, respectively, these techniques cannot track specific chemical elements. To investigate the role of Fe^{3+} in erythropoiesis, we need to combine capabilities for imaging elemental composition and three-dimensional (3-D) cellular ultrastructure at the nanoscale, but do not require high temporal resolution (Quiros et al., 2016; Valm et al., 2017). Here, we surmount this problem by combining two EM techniques that use scanned electron probes, which have the advantage of flexible detector geometry. We show that electron energy loss spectroscopy (EELS) imaging (Leapman, 2003; Fukunaga et al., 2010; Zhang et al., 2005) in the scanning transmission EM (STEM) (Hohmann-Marriott et al., 2009; Sousa and Leapman, 2009) combined with serial block-face scanning EM (SB-SEM) (Denk and Horstmann, 2004) (Figures 1 and S1) enables quantitative analysis of Fe^{3+} iron within specific organelles of cultured human hematopoietic CD34 + stem cells (Lee et al., 2013a, 2013b) that are undergoing erythropoiesis (Ganz and Nemeth, 2012; Moura et al., 2015). Erythropoiesis is the *in vivo* process (Hu et al., 2013; Orkin, 2000; Zivot et al., 2018; Notta et al., 2016) whereby stem cells terminally differentiate to erythrocytes, also known as red blood cells (RBCs), or to reticulocytes in the *ex vivo* cell cultures (Heshusius et al., 2019; Bernecker et al., 2019; Huang et al., 2014) investigated here. By sampling cells at different times in their path, from progenitor cells at $t_1 = 0$, through $t_2 = 7$ days and $t_3 = 14$ days, to reticulocytes at $t_4 = 21$ days, we investigate the precisely orchestrated process whereby iron finds its way into mitochondria from the labile iron pool to enable synthesis of heme (Muckenthaler et al., 2017), which is eventually incorporated into hemoglobin in the cytoplasm. Erythroblast differentiation *ex vivo* mimics the *in vivo* process, in which progenitor cells accumulate hemoglobin, eventually losing their nuclei and other organelles to form RBCs that fulfill these cells' primary function of oxygen transport through the vascular system.

It is known that mitochondria play a crucial role in supplying the cell's energy for every cell type, and in erythropoiesis, mitochondria perform another function in generating massive levels of heme (Chung et al., 2012; Chiabrando et al., 2014). Fluorescence and histochemical LM reveal that immature

[1]Laboratory of Cellular Imaging and Macromolecular Biophysics, National Institute of Biomedical Imaging and Bioengineering, NIH, Bethesda, MD, USA

[2]Penta Medix Co., Ltd., Seongnam, Gyeonggi-do, Republic of Korea

[3]National Institute of Diabetes and Digestive and Kidney Diseases, NIH, Bethesda, MD, USA

[4]Indiana Hemophilia and Thrombosis Center, Indianapolis, IN, USA

[5]Computational Biophysics, Center for Materials Physics and Technology, US Naval Research Laboratory, Washington, DC, USA

[6]Lead contact

*Correspondence: aronovaa@mail.nih.gov

https://doi.org/10.1016/j.isci.2021.102901

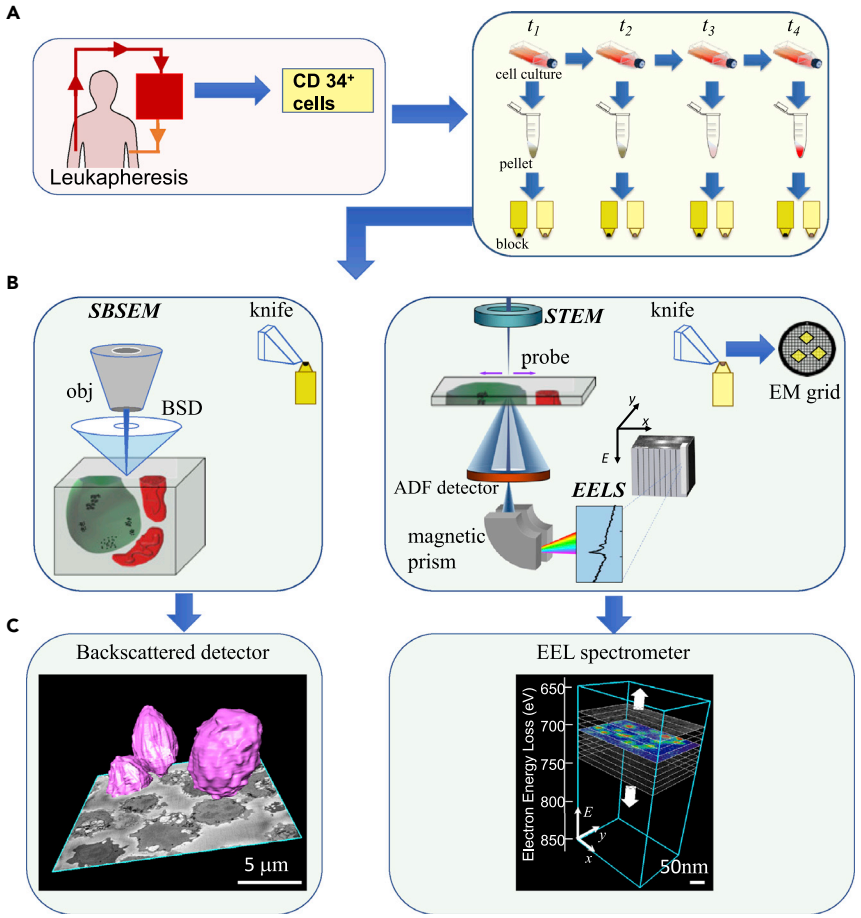

Figure 1. Workflow: sample collection/preparation, scanned probe set-up SB-SEM/STEM, and image analysis

(A) $CD34^+$ stem cells are isolated from healthy volunteers, via leukapheresis, and cultured in serum-free media. At 4 different time points of differentiation, t_1 = day 0, t_2 = day 7, t_3 = day 14 (7 days after erythropoietin [EPO] exposure), t_4 = day 19–21 (14 days after EPO exposure), cells are collected and pelleted, to undergo staining and embedding in preparation for electron microscopy (EM); two types of specimens are made with different staining protocols to accommodate the imaging techniques, and staining protocols are described in STAR Methods.

(B) Dual-electron beam techniques used to track morphological changes and Fe accumulation during erythropoiesis. Serial block-face scanning electron microscopy (SB-SEM): surface of plastic block containing embedded stained cells is scanned with focused electron probe, and image is collected with signal from backscattered electron detector; thin section is then removed from block with a diamond knife and block surface reimaged. This process is repeated until a stack containing hundreds of images is acquired. After image alignment, segmentation provides visualization and quantitation of organelle volumes (left). Scanning transmission electron microscopy (STEM): thin sections of embedded cells are deposited on TEM grids and imaged by using elastically scattered signal collected using an annular dark-field (ADF) detector, which reveals locations of heavy elements, or by using inelastically scattered signal collected using an electron energy loss spectrometer to obtain compositional information at a nanometer scale (right).

(C) Example of 3-D surface-rendered data, from images at t_3 stage, acquired with SB-SEM using a backscattered detector (left). Example of data acquired with STEM/EELS, using electron energy loss spectrometer, showing the cross section of region of a cell with identified quantifiable Fe distribution in ferritin molecules (right).

erythroblasts develop an organellar superstructure of mitochondria (Finsterer, 2007; Al-Mehdi et al., 2012; Green et al., 2011) surrounding iron-containing endolysosomes at the Golgi pole (Figure S2C [see black arrows], Figure S3). To interpret this dynamic morphology shift and its contribution to iron accumulation requires higher resolution imaging techniques (Figure 1). Although existence of lysosomal vesicles surrounded by mitochondria has been reported at the ultrastructural level during erythropoiesis (Sheftel et al., 2007; Miyamoto et al., 2011; Todkar et al., 2017), until now such morphology has only been observed in two-dimenstional thin sections using conventional TEM, and there has been no quantitative analysis of Fe^{3+} accumulation associated with the transport.

RESULTS

The complementarity of electron and light microscopy is underscored by a comparison between the information obtained from each approach. LM and STEM images both reveal changes in CD34 + cells as they differentiate from t_1 to t_4 (Figures S3A and S6A), during which mitochondria and membrane-bound lysosomes gather at the Golgi pole. In dark-field STEM images, where contrast originates from increased elastic scattering of heavier atoms, bright features ~10 nm in diameter within lysosomal compartments are attributed to iron-containing cores of ferritin molecules (Figures 2A and S6A); this is supported by the identification of ferritin light chain (FTL) in the same specimen areas as the lysosomal protein (LAMP1) in fluorescence optical images (Figure S3B). However, the colocalization of FTL with LAMP1 is not exact in the LM images because the ferritin occurs in clusters separated by as much as 500 nm, as seen in the STEM data at time t_2 in Figure S6A, which explains the more punctate distribution of FTL relative to LAMP1. In contrast, LAMP1 is more uniformly distributed than FTL in optical images because the vesicles are in closer proximity, typically separated by < 200 nm, and cannot be resolved in the LM images, also evident at time t_2 in Figure S6A. Not only can the STEM images provide the higher resolution ultrastructural information about the distribution of ferritin cores but also by combining STEM with EELS, we can obtain STEM-EELS maps (Pan et al., 2010) around the Fe $L_{2,3}$ edge resonance at ~710 eV (Figure 2B [left panel]), which confirms the presence of Fe^{3+} iron in each ferritin-core nanoparticle (Zega et al., 2003), as illustrated in the spectrum integrated over a single particle (Figure 2C [left panel]); variation in iron signal across different particles is also evident (Figure 2C [right panel]). If Fe^{2+} ions were present in the iron-containing nanoparticles, the Fe $L_{2,3}$ edge resonance at ~710 eV would be shifted to lower energy by 1 eV. The fact that this shift is not observed indicates that the iron is primarily in the Fe^{3+} and not Fe^{2+}state (Zega et al., 2003). Quantitative EELS analysis of 96 iron-containing particles (Figure 2B [right panel]) gives a mean Fe^{3+} content of 2,430 $\pm$ 820 ($\pm$s.d.) atoms, consistent with the known composition of isolated ferritin cores (Iancu, 1983; Bessis and Breton-Gorius, 1957) (Figure S4, STAR Methods). By counting the numbers of particles per unit area in STEM images of lysosomes and knowing the section thickness (~100 nm), we can estimate the number of ferritin cores and therefore the number of iron atoms per unit volume of lysosomes (STAR Methods). Then, from SB-SEM data, we can measure the volume of lysosomes per cell and accordingly the total number ferritin iron atoms per cell (Figure 3C [top panel], Figure S7).

Using the 3-D SB-SEM datasets, erythroblasts were segmented to obtain volumes of entire cells, nuclei, mitochondria, and lysosomes for 5 cells at each stage of development t_1-t_4 (Figures 3A and S5, Table S1, Video S1). Compartment volumes increase from t_1 to t_2, remain relatively constant up to t_3, and then decrease at t_4 (Figure 3B). The nuclear volume almost doubles from t_1 to t_2, elongating and developing invaginations to accommodate lysosome formation at the Golgi pole where mitochondria gather (Figures 3A, S3A, and S5). At t_4, nuclei become spherical with volumes fourfold lower than at t_3, before ejection. At t_1, few endolysosomes are evident, whereas at t_2 and t_3, the lysosomal volume increases more than 30-fold, which allows for iron storage. Finally, at t_4, organelles are digested via the autophagosomal pathway. Mitochondrial networks in close association with lysosomes mainly aggregate at the Golgi pole with formation of a side ridge. The mitochondrial volume increases twofold from t_1 to t_3, which accommodates greater heme production, after which the mitochondrial volume decreases, with eventual ejection of this organelle through autophagosomal digestion. The cell membrane is highly ruffled at t_1, t_2, and t_3 and becomes smooth only after organelles are digested and nucleus is extruded. Despite enucleation at t_4, terminally differentiated erythroblasts in *ex vivo* cultures resemble reticulocytes and do not form smooth biconcave discs characteristic of RBCs because they must enter the blood stream *in vivo* to fully mature (Figure 3A, lower panel). Nevertheless, our estimates of reticulocyte heme concentration match the known value for RBCs (Figure 3C [bottom]). Throughout t_1, t_2, and t_3 differentiation, cellular machinery must continue to produce massive amounts of heme and globin, even while the cell reorganizes.

By combining STEM-EELS with SB-SEM data, we can estimate the number of Fe^{3+} iron atoms within ferritin cores per cell at different stages of development (Figure 3C, [top panel]). Furthermore, we relate the number of Fe^{3+} iron atoms to heme production, which starts prior to t_3 and increases threefold at t_4 (Figure 3C, top panel). Our results show that ferritins accumulate in lysosomes, forming clusters as cells differentiate (Figure S6). From quantitative electron microscopy (Figures 3C, S7, and S9) and analytical biochemical analysis, we deduce that the iron stored in ferritin reaches a maximum of 1.8 $\pm$ 0.5 $\times$ 10^8 Fe^{3+} per cell at t_2, decreasing to 0.7 $\pm$ 0.3 $\times$ 10^8 Fe^{3+} per cell at t_3, before decreasing through continuing stages of differentiation as heme and hemoglobin accumulate, reaching a plateau in the reticulocyte at t_4*, which closely resembles the state of mature RBCs. Meanwhile, as the Fe^{3+} decreases, Figure 3C (lower panel) shows that

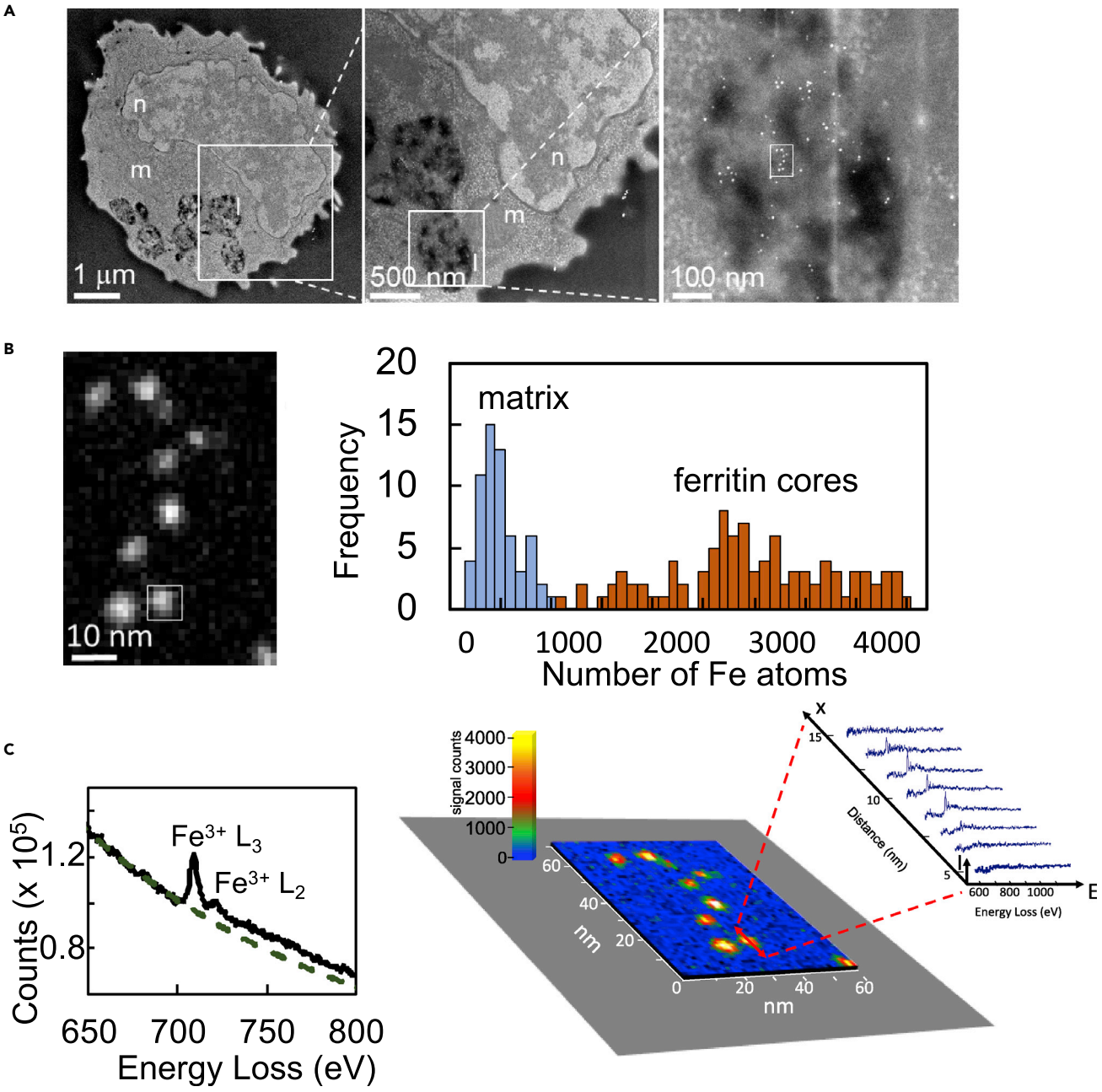

Figure 2. Imaging ferritin distributions in thin sections of differentiating erythroblasts with STEM/EELS

(A) ADF STEM images illustrated for a t_2 erythroblast: whole cell (left) with mitochondria (m) surrounding lysosomes (l) and invaginated by nucleus (n); magnified view (middle) shows proximity of lysosomes and mitochondrion; further magnification (right) shows identifiable individual ferritin cores inside lysosome. (B) Fe^{3+} mapping in ferritin cores of a small rectangular region, outlined in (A) (left panel).

(B) Fe distribution of individual ferritin cores found in lysosomes in 40 cells pooled for t_1-t_4 developmental stages together with the surrounding background measurements from other cellular regions (right panel). The average Fe content in the ferritin cores was found to be 2,429 $\pm$ 817 atoms, and the average in the surrounding background regions was -59 ± 195 atoms.

(C) EELS spectra (left panel) extracted and averaged over 6 x 6 pixels of one ferritin particle in (B), (white box), show peak at 710 eV corresponding to Fe^{3+} L_3 and Fe^{3+} L_2 edge. (C) (right panel) 2-D elemental map according to STEM/EELS Fe^{3+} signal (B) as function of *x* (position along sample), *E* (energy loss) and *I* (intensity, counts). As scan line is averaged over 6 pixels (in *y*) and scanned (along *x*, red double headed arrow) from top to bottom of a region containing a ferritin particle, the spectral shape in the vicinity of Fe^{3+} edge at 710 eV changes in intensity, depending on the Fe^{3+} content.

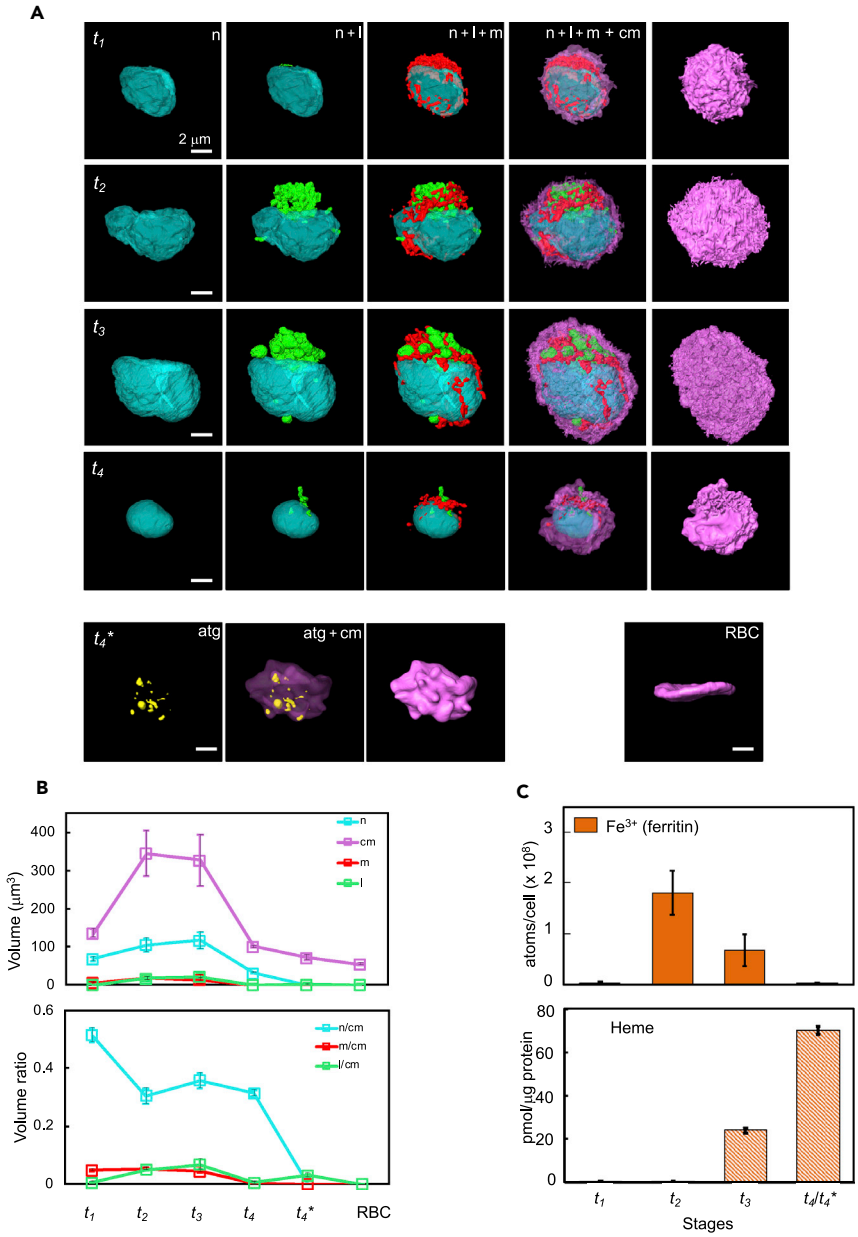

Figure 3. Morphological analysis of differentiating erythroblasts by SB-SEM reveals changes in organelle volumes and evolution of Fe^{3+} content; a model of cellular processes involved in erythropoiesis

(A) Surface rendering of SB-SEM segmented image data from representative cell at each development stage, t_1, t_2, t_3, and t_4 depicting evolution of cell morphology during erythroblast differentiation; cyan corresponds to nucleus (n), green, lysosomes (L), red, mitochondria (m), magenta, cell membrane (cm), and yellow, autophagosomes (atg). Lower row of images show t_4*, reticulocyte without nucleus, which resembles RBCs (shown for comparison at right) but with bumpy plasma membrane.

(B) Volume and volume fraction calculated from segmentation of each cellular development stage; standard errors of the mean from 5 different cells analyzed at each developmental stage are indicated (Table S1, Figure S5).

(C) Measured Fe^{3+} from ferritin in atoms per cell as a function of development stage (top); cellular heme measurements during t_1-t_4 culture period. Heme was measured as a portion of the total protein content (pmol/μg protein) (bottom). All error bars indicate standard deviation.

the heme content increases sharply to 70 pmol/μg of protein in the reticulocyte at t_4*. If it is assumed that reticulocytes have the same dry mass content as RBCs, i.e., 0.35 g dry mass of hemoglobin per ml of cell, and using the measured volume of 72 ± 12 μm^3 (Figure 3B), we find that each reticulocyte contains an

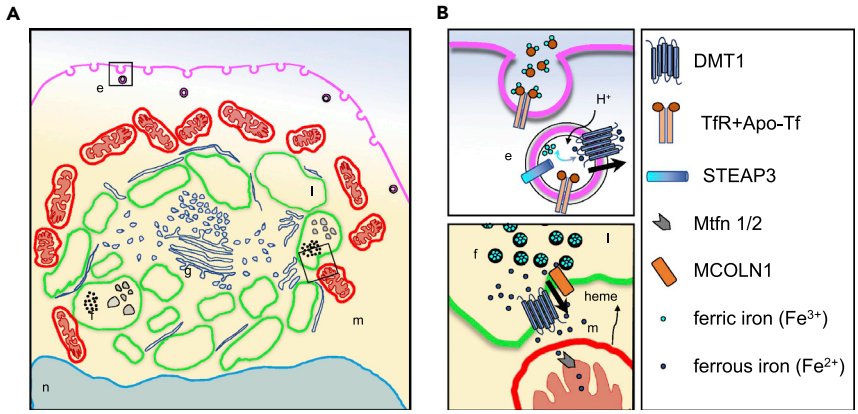

Figure 4. Proposed model describing iron trafficking during erythropoiesis based on existing knowledge and current findings

(A) Overall arrangement of organelles at t_2-t_3, which fascilitates production of heme via ferritin.

(B) Transferrin-receptor (TfR)-mediated endocytosis is used to capture extracellular ferric iron (Fe^{3+}) by binding to apo-transferrin (apo-Tf); intra-endosomal pH is lowered in endosomal vesicles, enabling dissociation of iron from transferrin and reduction of Fe^{3+} to Fe^{2+} through metalloreductase enzyme STEAP3; reduced Fe^{2+} iron exits endolysosomes via divalent metal transporter (DMT1) into cytoplasmic labile iron pool where it combines with Golgi-produced apo-ferritin shells and is oxidized back to Fe^{3+} to form crystalline ferritin cores. Subsequently, ferritin molecules together with other small vesicular bodies are engulfed by membranes via autophagosomal pathway into large lysosomes (L). We hypothesize that Fe^{2+} is trafficked via DMT1 or mucolipin-1 (MCOLN1) to mitochondria for inclusion into heme and iron-sulfur clusters through incompletely understood mechanisms.

average of 1.05 $\pm$ 0.17 $\times$ 10^9 Fe^{2+} in the form of heme, which is close to the value of 1.20 $\times$ 10^9 Fe^{2+} reported for a mature RBC (Lew at al., 1995). Continuous production of heme and hemoglobin during cell divisions after addition of erythropoietin (EPO) in erythropoiesis is well established (Lee et al., 2013a; Lee et al., 2013b), and it is known that loss of surface transferrin receptors does not occur until a state of terminal maturation is reached (Harding et al., 1983). Analysis of STEM tomograms and observation of a tight 5-10 nm apposition between mitochondrial and lysosomal membranes (Figure S8, Video S2) strongly support a hypothesis that transfer of Fe^{2+} occurs from ferritin stored in the lysosomes (Khalil et al., 2017) to mitochondria.

DISCUSSION

We base our model of ferritin's role in erythropoiesis on previously established models, developed by contributions of different reseachers over many years. We find direct evidence that ferritin plays a major role in the maturation of the RBC, a role that has previously been hypothesized (Philpott, 2018; Ryu et al., 2017) but not yet observed experimentally. We find from our structural analysis that this role of ferritin is accompanied by organellar rearrangements that occur during cellular differentiation and maturation of reticulocytes. In our model of iron uptake during erythroblast differentiation (Figure 4), transferrin-mediated endocytosis first captures extracellular Fe^{3+} into endosomal vesicles, whose pH are then lowered, allowing dissociation of Fe^{3+} from transferrin and reduction to Fe^{2+} (Fader and Colombo, 2006; Yamashiro et al., 1984). From our observation of highly ruffled cellular membrane and a threefold increase in cell volume from t_1 to t_3, we infer that increase in surface area may facilitate the docking of additional transferrin receptors carrying iron for heme production after they have been recycled back to the cell surface (Willingham et al., 1984). The reduced Fe^{2+} exits endolysosomes (Ohgami et al., 2006; Tabuchi et al., 2000) to the cytoplasmic labile iron pool where it combines with apoferritin. Fe^{2+} is then oxidized to Fe^{3+} in the ferritin cores, before being enclosed in larger lysosomal vesicles. Fe^{3+} is eventually converted back to Fe^{2+} and trafficked to mitochondria, which surround the lysosomes to enable heme production (Philpott, 2018; Ryu et al., 2017). This model suggests that dynamic morphological changes occur, involving mitochondria, lysosomes (Bogdan et al., 2016; Keerthivasan et al., 2010), Golgi, nuclear membrane, and plasma membrane, all of which play a crucial role in the maturation of cultured reticulocytes. As erythroblasts undergo terminal differentiation to reticulocytes, composed essentially of highly concentrated hemoglobin, they must continue to produce globin and heme in a milieu where much of the cellular machinery becomes increasingly impeded. From our observation, we suggest that only critical portions of the machinery remain: ribosomes

and mRNA for globin synthesis, mitochondria for heme synthesis, ATP molecules for energy, and iron storage by ferritin holoproteins sequestered in lysosomes, whose membranes eventually also function to expel the residual organelles from the cell. Because no macrophages are found in our *ex vivo* cell cultures, the ferritin that we observe in the differentiating erythroblasts cannot originate from pinocytosis following release of ferritin by macrophages (Leimberg et al., 2008). Our observations support an intimate relationship between erythropoiesis and iron homeostasis in differentiating erythroblasts, and we suggest a similar process occurs *in vivo* in maturing RBCs within bone marrow, although on a faster timescale (Porwit et al., 2011).

Thus, our results suggest a function for biology's natural hybrid nanoparticle, ferritin, in erythropoiesis, which in humans produces 2,000,000 new RBCs each second (Higgins, 2015). Perhaps this hitherto unknown role is not surprising because approximately 20–30% of the body's iron is stored as ferritin which is ubiquitous in every cell (Abbaspour et al., 2014; Finazzi and Arosio, 2014). A more complete understanding of iron processing at the subcellular level could elucidate *in vivo* erythropoiesis taking place in erythropoietic islands of bone marrow (Manwani and Beiker, 2008) as well as improve our ability to manufacture RBCs in *ex vivo* cultures, which could advance transfusion medicine (Douay, 2018).

Limitation of study

This study is limited by the use of CD34 + hematopoietic stem cells isolated from healthy human volunteers, via leukapheresis, and cultured in serum-free media. At 4 different time points of differentiation, t_1 = day 0, t_2 = day 7, t_3 = day 14 (7 days after EPO exposure), and t_4 = day 19–21 (14 days after EPO exposure), cells are collected and pelleted to undergo staining and embedding in preparation for EM.

STAR★METHODS

Detailed methods are provided in the online version of this paper and include the following:

- KEY RESOURCES TABLE
- RESOURCE AVAILABILITY
  - Lead contact
  - Materials availability
  - Data and code availability
- EXPERIMENTAL MODEL AND SUBJECT DETAILS
  - Cell cultures
- METHOD DETAILS
  - Reagents and antibodies
  - Sulfide-silver method (iron staining)
  - Measurement of heme and hemoglobin
  - Electron microscopy and SB-SEM
  - EM, STEM/EELS, and TEM
  - Ferritin standard and Fe^{3+} mapping
  - Movie generation
  - Calculation of cross section σ_{Fe} (β, Δ) for Fe $L_{2,3}$ white line
- QUANTIFICATION AND STATISTICAL ANALYSIS
  - Error generation for the number of Fe atoms
- ADDITIONAL RESOURCES

SUPPLEMENTAL INFORMATION

Supplemental information can be found online at https://doi.org/10.1016/j.isci.2021.102901.

ACKNOWLEDGMENTS

The Intramural Research Program of the National Institute of Biomedical Imaging and Bioengineering, the National Institute of Diabetes and Digestive and Kidney Diseases, and Office of Naval Research via the U.S. Naval Research Laboratory base program supported this work. We thank Dr. J. L. Miller for discussions on the topic of erythropoiesis.

AUTHOR CONTRIBUTIONS

RDL and MAA conceived and directed the project. MAA and SJN performed the experiments and analyzed the data. GZ prepared all electron microscopy specimens for both SB-SEM and STEM/EELS analysis. CB established primary cell culture and conducted flow cytometry analyses. ERM performed HPLC. YCK wrote and implemented MATLAB code to calculate atomic distributions. RDL, MAA, and SJN wrote and revised the final manuscript. Correspondence and requests for materials should be addressed to MAA or RDL. Supplemental information is available for this paper with initial submission.

DECLARATION OF INTERESTS

The authors declare no competing financial interests.

Received: February 8, 2021
Revised: June 8, 2021
Accepted: July 20, 2021
Published: August 20, 2021

SUPPORTING CITATIONS

The following references appear in the Supplemental Information: Brouzes and Asnafi, 2012; Maxfield and McGraw, 2004.

REFERENCES

Abbaspour, N., Hurrell, R., and Kelishadi, R. (2014). Review on iron and its importance for human health. J. Res. Med. Sci. *19*, 164–174.

Al-Mehdi, A.B., Pastukh, V.M., Swiger, B.M., Reed, D.J., Patel, M.R., Bardwell, G.C., Pastukh, V.V., Alexeyev, M.F., and Gillespie, M.N. (2012). Perinuclear mitochondrial clustering creates an oxidant-rich nuclear domain required for hypoxia-induced transcription. Sci. Signal. *5*, ra47.

Bernecker, C., Ackermann, M., Lachmann, N., Rohrhofer, L., Zaehres, H., Araúzo-Bravo, M.J., van den Akker, E., Schlenke, P., and Dorn, I. (2019). Enhanced ex vivo generation of erythroid cells from human induced pluripotent stem cells in a simplified cell culture system with low cytokine support. Stem Cells Dev. *28*, 1540–1551.

Bessis, M.C., and Breton-Gorius, J. (1957). Iron particles in normal erythroblasts and normal and pathological erythrocytes. J. Biophys. Biochem. Cytol. *3*, 503–504.

Bogdan, A.R., Miyazawa, M., Hashimoto, K., and Tsuji, Y. (2016). Regulators of iron homeostasis: new players in metabolism, cell death, and disease. Trends Biochem. Sci. *41*, 274–286.

Brouzes, C., and Asnafi, V. (2012). Erythroid leukemia evolving from multiple myeloma. Blood *119*, 2441.

Chiabrando, D., Mercurio, S., and Tolosano, E. (2014). Heme and erythropoieis: more than a structural role. Haematologica *99*, 973–983.

Chung, J., Chen, C., and Paw, B.H. (2012). Heme metabolism and erythropoiesis. Curr. Opin. Hematol. *19*, 156–162.

Denk, W., and Horstmann, H. (2004). Serial block-face scanning electron microscopy to reconstruct three-dimensional tissue nanostructure. PLoS Biol. *2*, e329.

Douay, L. (2018). Why industrial production of red blood cells from stem cells is essential for tomorrow's blood transfusion. Regen. Med. *13*, 627–632.

Egerton, R.F. (1979). K-shell ionization cross-sections for use in microanalysis. Ultramicroscopy *4*, 169–179.

Egerton, R.F. (2011). Electron Energy-Loss Spectroscopy in the Electron Microscope (Springer Science+Business Media).

Fader, C.M., and Colombo, M.I. (2006). Multivesicular bodies and autophagy in erythrocyte maturation. Autophagy *2*, 122–125.

Finazzi, D., and Arosio, P. (2014). Biology of ferritin in mammals: an update on iron storage, oxidative damage and neurodegeneration. Arch. Toxicol. *88*, 1787–1802.

Finsterer, J. (2007). Hematological manifestations of primary mitochondrial disorders. Acta Hematol. *118*, 88–98.

Fukunaga, M., Li, T.Q., van Gelderen, P., de Zwart, J.A., Shmueli, K., Yao, B., Lee, J., Maric, D., Aronova, M.A., Zhang, G., et al. (2010). Layer-specific variation of iron content in cerebral cortex as a source of MRI contrast. Proc. Natl. Acad. Sci. U S A *107*, 3834–3839.

Ganz, T., and Nemeth, E. (2012). Iron metabolism: interactions with normal and disordered erythropoiesis. Cold Spring Harb. Perspect. Med. *2*, a011668.

Green, D.R., Galluzzi, L., and Kroemer, G. (2011). Mitochondria and the autophagy-inflammation-cell death axis in organismal aging. Science *333*, 1109–1112.

Harding, C., Heuser, J., and Stahl, P. (1983). Receptor-mediated endocytosis of transferrin and recycling of the transferrin receptor in rat reticulocytes. J. Cell Biol. *97*, 329–339.

Heshusius, S., Heideveld, E., Burger, P., Thiel-Valkhof, M., Sellink, E., Varga, E., Ovchynnikova, E., Visser, A., Martens, J., von Lindern, M., and van den Akker, E. (2019). Large-scale in vitro production of red blood cells from human peripheral blood mononuclear cells. Blood Adv. *3*, 3337–3350.

Higgins, J.M. (2015). Red blood cell population dynamics. Clin. Lab. Med. *35*, 43–57.

Hohmann-Marriott, M.F., Sousa, A.A., Azari, A.A., Glushakova, S., Zhang, G., Zimmerberg, J., and Leapman, R.D. (2009). Nanoscale 3D cellular imaging by axial scanning transmission electron tomography. Nat. Methods *6*, 729–731.

Holcomb, P.S., Hoffpauir, B.K., Hoyson, M.C., Jackson, D.R., Deerinck, T.J., Marrs, G.S., Dehoff, M., Wu, J., Ellisman, M.H., and Spirou, G.A. (2013). Synaptic inputs compete during rapid formation of the calyx of Held: a new model system for neural development. J. Neurosci. *33*, 12954–12969.

Hu, J., Liu, J., Xue, F., Halverson, G., Reid, M., Guo, A., Chen, L., Raza, A., Galili, N., Jaffray, J., et al. (2013). Isolation and functional characterization of human erythroblasts at distinct stages: implications for understanding of normal and disordered erythropoiesis in vivo. Blood *121*, 3246–3253.

Huang, X., Shah, S., Wang, J., Ye, Z., Dowey, S.N., Tsang, K.M., Mendelsohn, L.G., Kato, G.J., Kickler, T.S., and Cheng, L. (2014). Extensive ex vivo expansion of functional human erythroid precursors established from umbilical cord blood cells by defined factors. Mol. Ther. *22*, 451–463.

Iancu, T.C. (1983). Iron overload. Mol. Aspects Med. *6*, 1–100.

Keerthivasan, G., Small, S., Liu, H., Wickrema, A., and Crispino, J.D. (2010). Vesicle trafficking plays a novel role in erythroblast enucleation. Blood *116*, 3331–3340.

Khalil, S., Holy, M., Grado, S., Fleming, R., Kurita, R., Nakamura, Y., and Goldfarb, A. (2017). A specialized pathway for erythroid iron delivery through lysosomal trafficking of transferrin receptor 2. Blood Adv. *1*, 1181–1194.

Leapman, R.D. (2003). Detecting single atoms of calcium and iron in biological structures by electron energy-loss spectrum-imaging. J. Microsc. *210*, 5–15.

Lee, Y.T., Kim, K.S., Byrnes, C., de Vasconcellos, J.F., Noh, S.J., Rabel, A., Meier, E.R., and Miller, J.L. (2013a). A synthetic model of human beta-thalassemia erythropoiesis using CD34+ cells from healthy adult donors. PLoS One *8*, e68307.

Lee, Y.T., de Vasconcellos, J.F., Yuan, J., Byrnes, C., Noh, S.J., Meier, E.R., Kim, K.S., Rabel, A., Kaushal, M., Muljo, S.A., and Miller, J.L. (2013b). LIN28B-mediated expression of fetal hemoglobin and production of fetal-like erythrocytes from adult human erythroblasts ex vivo. Blood *122*, 1034–1041.

Leimberg, M.J., Prus, E., Konijn, A.M., and Fibach, E. (2008). Macrophages function as a ferritin iron source for cultured human erythroid precursors. J. Cell. Biochem. *103*, 1211–1218.

Lew, V.L., Raftos, J.E., Sorette, M., Bookchin, R.M., and Mohandas, N. (1995). Generation of normal human red cell volume, hemoglobin content, and membrane area distributions by "birth" or regulation? Blood *86*, 334–341.

Manwani, D., and Bieker, J.J. (2008). The erythroblastic island. Curr. Top. Dev. Biol. *82*, 23–53.

Maxfield, F.R., and McGraw, T.E. (2004). Endocytic recycling. Nat. Rev. Mol. Cell Biol. *5*, 121–132.

Miyamoto, Y., Kitamura, N., Nakamura, Y., Futamura, M., Miyamoto, T., Yoshida, M., Ono, M., Ichinose, S., and Arakawa, H. (2011). Possible existence of lysosome-like organella within mitochondria and its role in mitochondrial quality control. PLoS One *6*, e16054.

Moura, I.C., Hermine, O., Lacombe, C., and Mayeux, P. (2015). Erythropoiesis and transferrin receptors. Curr. Opin. Hematol. *22*, 193–198.

Muckenthaler, M.U., Rivella, S., Hentze, M.W., and Galy, B. (2017). A red carpet for iron metabolism. Cell *168*, 344–361.

Notta, F., Zandi, S., Takayama, N., Dobson, S., Gan, O.I., Wilson, G., Kaufmann, K.B., McLeod, J., Laurenti, E., Dunant, C.F., et al. (2016). Distinct routes of lineage development reshape the human blood hierarchy across ontogeny. Science *351*, aab2116.

Ohgami, R.S., Campagna, D.R., McDonald, A., and Fleming, M.D. (2006). The Steap proteins are metalloreductases. Blood *108*, 1388–1394.

Orkin, S.H. (2000). Diversification of haematopoietic stem cells to specific lineages. Nat. Rev. Genet. *1*, 57–64.

Pan, Y.-H., Vaughan, G., Brydson, R., Bleloch, A., Gass, M., Sader, K., and Brown, A. (2010). Electron-beam-induced reduction of Fe3+ in iron phosphate dihydrate, ferrihydrite, haemosiderin and ferritin as revealed by electron energy-loss spectroscopy. Ultramicroscopy *110*, 1020–1032.

Philpott, C.C. (2018). The flux of iron through ferritin in erythrocyte development. Curr. Opin. Hematol. *25*, 183–188.

Porwit, A., McCullough, J., and Erber, W.E. (2011). Blood and Bone Marrow Pathology (Elsevier).

Quirós, P.M., Mottis, A., and Auwerx, J. (2016). Mitonuclear communication in homeostasis and stress. Nat. Rev. Mol. Cell Biol. *17*, 213–226.

Regan, T.J., Ohldag, H., Stamm, C., Nolting, F., Lüning, J., Stöhr, J., and White, R.L. (2001). Chemical effects at metal/oxide interfaces studied by x-ray-absorption spectroscopy. Phys. Rev. B *64*, 214422.

Ryu, M.S., Zhang, D., Protchenko, O., Shakoury-Elizeh, M., and Philpott, C.C. (2017). PCBP1 and NCOA4 regulate erythroid iron storage and heme biosynthesis. J. Clin. Invest. *127*, 1786–1797.

Sheftel, A.D., Zhang, A.S., Brown, C., Shirihai, O.S., and Ponka, P. (2007). Direct interorganellar transfer of iron from endosome to mitochondrion. Blood *110*, 125–132.

Sousa, A.A., and Leapman, R.D. (2012). Development and application of STEM for the biological sciences. Ultramicros *123*, 38–49.

Tabuchi, M., Yoshimori, T., Yamaguchi, K., Yoshida, T., and Kishi, F. (2000). Human NRAMP2/DMT1, which mediates iron transport across endosomal membranes, is localized to late endosomes and lysosomes in HEp-2 cells. J. Biol. Chem. *275*, 22220–22228.

Todkar, K., Ilamathi, H.S., and Germain, M. (2017). Mitochondria and lysosomes: discovering Bonds. Front. Cell Dev. Biol. *5*, 1–7.

Utlaut, M. (1981). Comparison of Electron and Photon Beams for Obtaining Inner Shell Spectra. EXAFS Spectroscopy: Techniques and Applications (Springer Science+Business Media New York).

Valm, A.M., Cohen, S., Legant, W.R., Melunis, J., Hershberg, U., Wait, E., Cohen, A.R., Davidson, M.W., Betzig, E., and Lippincott-Schwartz, J. (2017). Applying systems-level spectral imaging and analysis to reveal the organelle interactome. Nature *546*, 162–167.

Walton, J. (1979). Lead aspartate, an en bloc contrast stain particularly useful for ultrastructural enzymology. J. Histochem. Cytochem. *27*, 1337–1342.

West, J.B., Fu, Z., Deerinck, T.J., Mackey, M.R., Obayashi, J.T., and Ellisman, M.H. (2010). Structure-function studies of blood and air capillaries in chicken lung using 3D electron microscopy. Resp. Phys. Neurobiol. *170*, 202–209.

Willingham, M.C., Hanover, J.A., Dickson, R.B., and Pastan, I. (1984). Morphologic characterization of the pathway of transferrin endocytosis and recycling in human KB cells. Proc. Natl. Acad. Sci. U S A *81*, 175–179.

Wojda, U., Noel, P., and Miller, J.L. (2002). Fetal and adult hemoglobin production during adult erythropoiesis: coordinate expression correlates with cell proliferation. Blood *99*, 3005–3013.

Yamashiro, D.J., Tycko, B., Fluss, S.R., and Maxfield, F.R. (1984). Segregation of transferrin to a mildly acidic (pH 6.5) para-Golgi compartment in the recycling pathway. Cell *37*, 789–800.

Zdolsek, J.M., Roberg, K., and Brunk, U.T. (1993). Visualization of iron in cultured macrophages - a cytochemical light and electron-microscopic study using autometallography. Free Rad. Biol. Med. *15*, 1–11.

Zega, T.J., Garvie, L.A.J., and Buseck, P.R. (2003). Electron energy-loss spectroscopy (EELS) of Fe-bearing sheet silicates in CM chondrites. Lunar Plan. Sci. *34*, 2089.

Zhang, P., Land, W., Lee, S., Juliani, J., Lefman, J., Smith, S.R., Germain, D., Kessel, M., Leapman, R., Rouault, T.A., and Subramaniam, S. (2005). Electron tomography of degenerating neurons in mice with abnormal regulation of iron metabolism. J. Struct. Biol. *150*, 144–153.

Zivot, A., Lipton, J.M., Narla, A., and Blanc, L. (2018). Erythropoiesis: insights into pathophysiology and treatments in 2017. Mol. Med. *24*, 11.

STAR★METHODS

KEY RESOURCES TABLE

REAGENT or RESOURCE	SOURCE	IDENTIFIER
Antibodies		
Anti-TFR2 antibody	Santa Cruz Biotechnology	sc-376278; RRID:AB_11008080
Anti-Giantin antibody	Abcam	ab174655
Anti-LAMP1 antibody	Abcam	ab24170; RRID:AB_775978
Anti-gamma tubulin antibody	Abcam	ab11317; RRID:AB_297921
Anti-FTL antibody	Abcam	ab69090; RRID:AB_1523609
Anti-Rab11 antibody	Millipore	Cat # 05-853
Anti-DDK antibody	Origene	Cat # TA50011-100; RRID:AB_2622345
Alexa Fluor™ 594 labeled Transferin	Thermo Fisher Scientific	Cat #T13343
Biological samples		
ex vivo for 21 days, four cell populations were isolated: t_1[CD34(+)], t_2 [CD36(+), CD235(−) erythroblast], t_3 [CD36(+), CD235(+) erythroblast], and t_4 (nucleated and enucleated erythrocytes)	This paper	NA
Chemicals, peptides, and recombinant proteins		
Paraformaldehyde	EMS	RT15712
L-Glutamine	Thermo Fisher Scientific	Cat # 21051024
Pen-strep	Thermo Fisher Scientific	Cat # 15070063
StemPro™-34 SFM	Thermo Fisher Scientific	Cat # 10639011
SCF	Proteintech	Cat # HZ-1024
FLT3 Ligand	Proteintech	Cat # HZ-1151
IL-3	Proteintech	Cat # HZ-1074
Mifepristone	Sigma Aldrich	Cas # 84371-65-3
Insulin	Sigma Aldrich	Cas # 11061-68-0
Holo-transferrin	Sigma Aldrich	Cas # 11096-37-0
Glutaraldehyde	Sigma Aldrich	Cas # 111-30-8
Sodium cacodylate trihydrate	Sigma Aldrich	Cas # 6131-99-3
Thiocarbohydrizide (TCH)	EMS	Cat # 21900
Osmium tetroxide	EMS	Cas # 20816-12-0
Epon-Araldite	EMS	Cat #13940
CircuitWorks Conductive Epoxy	Chemtronics	CW2400
Ferritin from equine spleen	Sigma Aldrich	F4503-25MG
Experimental models: cell lines		
CD34 + stem cells	This paper	NA
Software and algorithms		
Amira (v2020.2)	Thermo Fisher Scientific	http://www.fei.com/software/amira-3d-for-life-sciences/
MATLAB (2019b)	Mathworks	http://www.mathworks.com/products/matlab/
Digital Micrograph (GMS3)	Gatan	https://www.gatan.com/products/tem-analysis/gatan-microscopy-suite-software
IMOD	University of Colorado	https://bio3d.colorado.edu/imod/

RESOURCE AVAILABILITY

Lead contact

Maria A. Aronova: aronovaa@mail.nih.gov.

Further information and requests for resources and reagents should be directed to and will be fulfilled by the lead contact, Maria A. Aronova: aronovaa@mail.nih.gov.

Materials availability

No materials were generated in this study that need to be made available. This study did not generate new unique reagents, and there are no restrictions to availability.

Data and code availability

No new code was used in this study. Any additional information regarding data or data analysis reported in this paper can be available from the lead contact upon request.

EXPERIMENTAL MODEL AND SUBJECT DETAILS

Cell cultures

All studies involving human subjects were approved by the Institutional Review Board of the National Institute of Diabetes and Digestive and Kidney Diseases. After informed consent was obtained, human CD34(+) cells were collected from peripheral blood of healthy volunteers at the National Institutes of Health (Bethesda, MD). Using primary human CD34 + stem cells, which were isolated via leukapheresis (Figure 1A) and cultured *ex vivo* for 21 days, four cell populations were isolated: t_1[CD34(+)], t_2 [CD36(+), CD235(−) erythroblast], t_3 [CD36(+), CD235(+) erythroblast], and t_4 (nucleated and enucleated erythrocytes) (Lee et al., 2013a, 2013b). In summary, a 21-day *ex vivo* serum-free culture system was used; in culture days 1–7, CD34 + cells were placed in media containing StemPro-34 complete media (l-glutamine, pen-strep and StemPro-34 nutrient supplement, Invitrogen, Carlsbad, CA) supplemented with 50 ng/mL of SCF (HumanZyme, Chicago, IL), 50 ng/mL of FLT3-Ligand (HumanZyme), and 10 ng/mL of IL-3 (HumanZyme). After 7 days, the cells were transferred to EPO (Amgen)-supplemented medium. Culture days 7–21 was comprised of the following: StemPro-34 complete medium, 4 U/ml EPO, 3 μM mifepristone (Sigma Aldrich, St. Louis, MO), 10 μg/mL insulin (Sigma Aldrich), 3 U/ml heparin (Hospira, Inc, Lake Forest, IL), and 0.8 mg/mL holo transferrin (Sigma Aldrich). Overall, primary erythroblasts in culture demonstrated well-coordinated cellular events including transferrin receptor upregulation and increased heme and hemoglobin production that are largely mediated by EPO (Figure S2).

METHOD DETAILS

Reagents and antibodies

The following reagents/primary antibodies were used for immunofluorescence analyses: paraformaldehyde solution (10%) (EMS, Hatfield, PA); mouse anti-TfR2, rabbit anti-DMT1 (Santa Cruz Biotechnology, Santa Cruz, CA); rabbit anti-lysosomal-associated membrane protein 1 (LAMP1), rabbit anti-Giantin, rabbit anti-γ-tubulin, rabbit polyclonal anti-FTL (Abcam, Cambridge, MA); mouse anti-Rab11 (Millipore, Billerica, MA); mouse anti-DDK (4C5) (OriGene Technologies, Rockville, MD). Alexa-594-labeled transferrin, Mitotracker Red, and Alexa-488- or Alexa-594-labeled anti-mouse IgG or anti-rabbit IgG secondary antibodies were from Invitrogen (Carlsbad, CA). Mounting medium for fluorescence with DAPI staining was purchased from Vector Laboratories (Burlingame, CA).

Sulfide-silver method (iron staining)

Initial studies of intracellular iron were performed by sulfide-silver staining as previously described (Zdolsek et al., 1993). All chemicals used in sulfide-silver staining were obtained from Sigma Aldrich. In brief, cells were fixed with 2% glutaraldehyde in 0.1 M Na-cacodylate (pH 7.2) with 0.1 M sucrose for up to 2 hr at room temperature. After washing 5 times with H_2O, samples were sulphidated with 1% ammonium sulphide (pH ~9) in 70% ethanol for 15 min and then washed with H_2O. Heavy metals (mainly iron in cells) were visualized by autometallography in a colloid-protected developer containing silver nitrate and hydroquinone in citrate buffer in the dark for 20 to 30 min.

Measurement of heme and hemoglobin

The QuantiChrom heme Assay (BioAssay Systems) was used to measure heme in cultured erythroid cell lysates (t_1-t_4). The amount of heme in each sample was normalized per microgram of total protein. Hemoglobin in erythroid cells at t_2 and t_4 (2 million cells each) was detected by high-performance liquid chromatography (HPLC) as previously described (Wojda et al., 2002). In short, the cells were lysed in deionized sterile water, by repeated freezing and thawing, and then pelleted by brief centrifugation. The supernatants then were filtered through Ultrafree-MC devices (Millipore, Bedford, MA) before cation-exchange chromatography. Hemoglobin from cell lysates was separated on a 20 × 4-mm POLYCATA column (PolyLC, Columbia, MD) fitted to a Gilson HPLC system (Gilson, Middleton, WI) and then eluted during 4-min 8%–40% gradient of buffer B (20 mM Bis-Tris, 2 mM KCN, 200 mM NaCl, pH 6.55) in buffer A (20 mM Bis-Tris, 2 mM KCN, pH 6.96) according to the manufacturer's protocol. Hemoglobin protein was detected by absorbance measurements at 415 nm. Direct quantitation of hemoglobin was conducted by integration of the areas under the HbA peak using software supplied by the manufacturer.

Electron microscopy and SB-SEM

Combinatorial heavy-metal staining protocol was followed, developed by Mark Ellisman's group (Holcomb et al., 2013; West et al., 2010). The cells from 4 developmental stages, t_1 = day 0, t_2 = day 7, t_3 = day 14 (7 days after EPO exposure), t_4 = day 19–21 (14 days after EPO exposure), were fixed for five minutes in a mixture of 2.5% glutaraldehyde and 2% formaldehyde in sodium cacodylate buffer with 2 mM calcium chloride. Then they were fixed for another two to three hours on ice in the same solution, after which they were rinsed (2x or 3x) with cold cacodylate buffer containing 2 mM calcium chloride (five minutes for each rinse). For heavy-metal staining, the cells were fixed in reduced osmium—a solution containing 3% potassium ferricyanide in 0.3 M cacodylate buffer with 4 mM calcium chloride combined with an equal volume of 4% aqueous osmium tetroxide—for one hour on ice. They were then placed in a 0.22-μm Millipore-filtered 1% thiocarbohydrazide solution in ddH_2O for 20 min. The heavy-metal staining phase concluded with fixation of the samples in 2% osmium tetroxide in ddH_2O for 30 min. Between each of the preceding steps, the samples were washed five times, three minutes each time, with ddH_2O. At last, the samples were placed in 1% aqueous uranyl acetate and left overnight at ~4°C. The next day, after once again washing the samples with ddH_2O five times for three minutes each time, we performed *en bloc* Walton's lead aspartate staining (Walton, 1979): the cells were submerged in a lead aspartate solution and placed in the oven for 30 min at 60°C. Then, following another five three-minute ddH_2O rinses, the samples were dehydrated and embedded in Epon-Araldite (EMS, Hatfield, PA) according to standard protocols. The final sample preparation step was to mount the embedded cells for SB-SEM with the goal of minimizing specimen charging. Each resin-embedded sample was first mounted on an empty resin block to be trimmed under the microtome. Once its top was exposed, each block was remounted, exposed side down, to a special aluminum specimen pin (Gatan, Pleasanton, CA) using CircuitWorks Conductive Epoxy (CW2400); CW2400 served to electrically ground the cells to the aluminum pin. The remounted samples were then trimmed again, and, finally, sputter-coated with a thin ~4-nm layer of gold.

The trimmed resin-embedded stained cells were imaged using a Gatan 3View serial block-face imaging system installed on a Zeiss SIGMA-VP SEM, operating at an accelerating voltage of 2.7 kV using a 60-μm condenser aperture. The SEM was operated at 25-Pa gas pressure. The acquired images had a pixel size of 7.7 nm in the x-y plane and 50 nm along the z axis. The resulting datasets were assembled into volume files and aligned using Digital Micrograph (Gatan, Inc.), binned by 4, and then manually segmented into 3-D models in Amira (FEI, Thermo Fisher Scientific). Some thresholding was used to expedite the process. The volumes of the segmented organelles mitochondria, nuclei, vesicles, and cell membrane were measured using Amira software's "Material Statistics" module, thus obtaining all the reported 3-D size parameters. Measurements were obtained from 27 cell membranes, 21 nuclei, 20 mitochondrial networks, and 25 vesicle networks, with 5 cells selected from each of the 4 developmental stages. All cell-type differentiation was performed by visual inspection, and cell types were assessed according to established morphologies (Hu et al., 2013).

EM, STEM/EELS, and TEM

For STEM/EELS, cells from different time stages were pelleted and fixed in a mixture of 2.5% formaldehyde and 2.0% glutaraldehyde in phosphate buffered saline (PBS) (pH = 7.4), followed by 0.02% osmium tetroxide fixation for 1 hr. After several rinses in the buffer (3 × 10 min), the samples were dehydrated in a series of ethanol (20%, 40%, 60%, 75%, and 95% for 10 min and 100% for 30 min with 3 changes) and infiltrated with

Epon-Araldite for 2 days (25% of Epon-Araldite and ethanol for 2h, 50% for 4h, 75% for 8h, and 100% for 1 day with 2 changes). The samples were polymerized at 60°C for 2 days.

The TEM/STEM samples that were not analyzed by EELS and were only used for structural evaluation were prepared by fixing cells in a mixture of 2.5% formaldehyde and 2.0% glutaraldehyde, briefly rinsed in 0.1 M sodium cacodylate buffer, and postfixed in 1.0% osmium tetroxide plus 0.8% potassium ferricyanide in the same buffer for 60 min. After several rinses in PBS (3x for 10 min), the samples were dehydrated in an ethanol gradient as mentioned earlier for the EELS preparation and infiltrated with Epon-Araldite for a couple days. The samples were then polymerized at 60°C for another 2 days. For all different time stages, the samples were prepared and imaged the same way. Sections of thickness 100-120 nm were deposited on TEM copper girds.

Ferritin standard and Fe^{3+} mapping

To compare results with a pure ferritin-standard sample, horse spleen ferritin (Sigma-Aldrich, US) was deposited on a thin carbon film (~5 nm) and was let to dry.

Dark-field STEM and STEM/EELS images were acquired using Tecnai TF30 electron microscope (FEI, Thermo Fisher Scientific), equipped with a Quantum imaging filter (Gatan Inc., Warrendale, PA), and operating at an accelerating voltage of 300 kV. The energy loss range was 445 eV–1470 eV, and the elemental maps were taken from a small area of the specimen, using drift correction when needed. Elemental images containing about 50 by 50 pixels were acquired with a pixel size of 1–2 nm.

To determine the iron loading in the ferritin particles (standard sample) after imaging with STEM/EELS, the spectral tool in the Digital Micrograph software (Gatan Inc.) was used to select individual ferritin particles. The background under the Fe $L_{2,3}$ core edge at 710 eV was removed by fitting the inverse power law (Leapman, 2003), and the Fe $L_{2,3}$ signal was summed over a 10-eV window, to generate an integrated Fe signal map. The iron map was quantified by dividing the net Fe signal by the product of inelastic cross section and the total beam current. Thus, the number of Fe atoms N_{Fe} in each analyzed ferritin particle was calculated according to the following: $N_{Fe} = d^2 \times S_{Fe}(\beta,\Delta)/I_0\sigma_{Fe}(\beta,\Delta)$, where S_{Fe} is signal (the number of counts in the Fe L edge), I_0 is the total incoming current (the number of counts in the zero loss and low-loss spectrum), σ_{Fe} is the inelastic cross section, and d is the pixel size in nm. β is the collection semiangle defined by the spectrometer entrance aperture, which was 20 mrad, and Δ is the integration energy window, which was set to be 10 eV in order to include the L_3 white line resonance. A value for the scattering cross section σ_{Fe} is not well established with a wide range of values reported in previous literature. We have therefore calculated the L_3 white line cross section both from X-ray data and from empirical EELS measurements on nanoparticles of known composition. The value used here for $\sigma_{Fe}(\beta, \Delta)$ was estimated to be (1.46 $\pm$ 1.3) x 10^{-7} nm^2/atom ($\overline{x} \pm$ SEM).

Movie generation

Videos S1 and S2 are made in Amira software that allows the observer to go through the 3-D data in the form of orthoslices and view the surface/volume rendered models for further analysis.

Calculation of cross section σ_{Fe} (β, Δ) for Fe $L_{2,3}$ white line

The cross section was calculated in two ways.

1. The relation between photoabsorption cross section and the nonrelativistic electron energy loss differential cross section is given by Utlaut, 1981:

$$\frac{\sigma_\gamma(E)}{\left[\frac{d\sigma(E)}{dE}\right]} = \frac{2\pi a_0}{\hbar c}\frac{E_0 E}{ln\left[\frac{4E_0}{E}\right]}, \qquad \text{(Equation 1)}$$

where E is the photon energy or energy loss, E_0 is the primary electron energy, a_0 is the Bohr radius, $\hbar$ Plank's constant divided by 2π, c is the speed of light, and $\frac{d\sigma(E)}{dE}$ is the electron energy loss differential cross section. Using the relativistically corrected beam energy T_0 instead of E_0, we can write

$$\left[\frac{d\sigma(E)}{dE}\right] = ln\left[\frac{4T_0}{E}\right]\left[\frac{1}{1.68 \times 10^{-3}T_0}\right]\frac{\sigma_\gamma(E)}{[E]}, \quad \text{(Equation 2)}$$

Experimental X-ray absorption data measure absorption coefficient $\mu(E)$ instead of absorption cross section $\sigma_\gamma(E)$:

$$\mu(E) = n\sigma_\gamma(E), \quad \text{(Equation 3)}$$

where n is the number of atoms of element per unit volume. Now considering the Fe L_3 white line excitation at 708 $\pm$ 5 eV and integrating the photoabsorption spectrum and the electron energy loss spectrum, for an incident electron energy of E_0 = 300 keV or T_0 = 154.1 keV (Egerton, 2011), then,

$$\int \frac{d\sigma(E)}{dE}dE = \frac{0.0262}{nE_{Fe-white\ line}}\int \mu(E)dE, \quad \text{(Equation 4)}$$

$$n = \frac{\rho_{Fe}N_0}{A_{Fe}}, \quad \text{(Equation 5)}$$

where ρFe is the density of Fe, N_0 is the Avogadro's number, and AFe is the atomic weight of Fe. From these constants, n is calculated to be 85 Fe atoms/nm^3

$$\int \frac{d\sigma(E)}{dE}dE = \frac{0.0262}{n}\int \mu(E)dE = 1.17 \times 10^{-7} nm^2 \Big/ atom,$$

The integral of $\mu(E)$ is obtained from published X-ray absorption data (Regan et al., 2001) with an estimated uncertainty of 5%. Therefore, $\boldsymbol{\sigma_{Fe}}$ **= (1.17 $\pm$ 0.06) $\times 10^{-7}$ nm^2/atom**

2. We calculate σ_{Fe} using experimental data from material of a known composition containing Fe: Fe_2O_3 and Fe_3O_4 nanoparticles. We can write

$$N_{Fe} = \left(\frac{S_{Fe}(\beta,\Delta)}{I_0\sigma_{Fe}(\beta,\Delta)}\right) * d^2\ N_O = \left(\frac{S_O(\beta,\Delta)}{I_0\sigma_O(\beta,\Delta)}\right) * d^2, \quad \text{(Equation 6)}$$

$$\frac{N_O}{N_{Fe}} = \frac{S_O(\beta,\Delta)\ \sigma_{Fe}(\beta,\Delta)}{\sigma_O(\beta,\Delta)S_{Fe}(\beta,\Delta)}, \quad \text{(Equation 7)}$$

Here, S_{Fe} and S_O are integrated signals for iron and oxygen, respectively, I_0 is the total incoming electron dose, σ_{Fe}/σ_O is the inelastic cross section for Fe/O, and d is the pixel size in nm. β is the collection semiangle defined by the spectrometer entrance aperture, which was 20 mrad and Δ is the integration energy window, which is 10 eV for Fe and 100 eV for oxygen. Knowing the σ_O and the ratio of elements found in the material, we can solve for σ_{Fe}.

To find out σ_O at beam energy of 300 keV, we use data from Egerton R. F (Egerton, 1979) for σ_O at beam energy of 100 keV = 3.5x10^{-7} nm^2/atom and Equation 2.

$$\frac{\sigma_{O,E=300keV}}{\sigma_{O,E=100keV}} = f,\ f = \frac{T_0(100\ keV)}{T_0(300\ keV)}\frac{ln\left[\frac{4E_0(300keV)}{580}\right]}{ln\left[\frac{4E_0(100keV)}{580}\right]}, \quad \text{(Equation 8)}$$

where the calculated f is 0.581, which gives rise to σ_O at 300 keV = 2.03 x 10^{-7} nm^2/atom.

By analyzing 23 particles, the σ_{Fe} = (1.46 $\pm$ 0.13) $\times 10^{-7}$ nm^2/atom ($\bar{x} \pm$SEM)

QUANTIFICATION AND STATISTICAL ANALYSIS

Error generation for the number of Fe atoms

To generate distributions and their respective errors of the number of Fe atoms per cell at stages t_1-t_4 as shown in Figure 3C, the following calculations were performed on the ADF STEM thin-section images, for t_1 and t_2 specimens, because the ferritin particles were found in most lysosomes, we used a statistical approach to obtain the total number of ferritins found in a cell fer^{cell},

$$fer^{cell} = \frac{\sum fer^{lys}}{\sum A^{lys} * t} \times V^{lys} \quad \text{(Equation 9)}$$

in which $\sum fer^{lys}$ is the total number of ferritins found in the lysosomal region per cell in a thin section, $\sum A^{lys}$ is the total area of the lysosomes in nm^2 in a thin section per cell, t is the section thickness in nm, which is 100 nm, and V^{lys} is the total lysosomal volume in nm^3, a measurement that is only obtainable from segmented volume, of SB-SEM data. There were 150–200 lysosomal areas analyzed for t_1-t_4 specimens. The values used to plot the histogram in Figure 3 are $\overline{fer}^{cell} \pm$ s.e.m.

For t_3 and t_4 stages, because most of the lysosomes did not contain ferritins and the ones that did formed stochastic clusters, we approached the analysis differently in order to propagate the error that is meaningful. First, we obtain the volume of ferritin clusters V^{clus}:

$$V^{clus} = \frac{\sum A^{clus}}{\sum A^{lys} * t} \times V^{lys} \quad \text{(Equation 10)}$$

where $\sum A^{clus}$ is the summation of all the areas that the clusters occupy in nm^2 in a cell of the thin section, $\sum A^{lys}$ is the total area of the lysosomes in nm^2 in the same cell of a thin section, t is the section thickness in nm, which is 100 nm, and V^{lys} is the total lysosomal volume in nm^3, a measurement that is only obtainable from segmented volume of SB-SEM data. From the ferritin clusters that were observed, we obtained the average number of ferritins per cluster – fer^{clus}. Therefore, the total number of ferritins in a cell fer^{cell} is

$$fer^{cell} = fer^{clus} \times V^{clus}, \quad \text{(Equation 11)}$$

We have propagated the error for each of these operations. The area fraction's $\frac{\sum A^{clus}}{\sum A^{lys}}$ s.e.m. error was used because there is a large lysosome to lysosome variability. As a result of these calculations, the graphs for Figure S7 are generated.

ADDITIONAL RESOURCES

Our study has not generated or contributed to a new website/forum, and it is not part of a clinical trial.